

Hybrid Electrospun Nanofibers as Electrocatalyst for Vanadium Redox Flow Batteries: Theory and Experiment

Mahboubeh Maleki,^{*[a]} Tim Tichter,^[a] Gumaa A. El-Nagar,^[a, b, c] Iver Lauermaann,^[c] and Christina Roth^[a, d]

Selective modification of the morphology and intrinsic electrocatalytic activity of porous electrodes is urgently required to improve the performance of vanadium redox flow batteries (VRFBs). For this purpose, electrospinning was exploited to prepare high-performance nanofiber-based composites. Blends of polyacrylonitrile, polyacrylic acid, and polyaniline with carbon black were electrospun into a 3D free-standing nanofibrous web, which was utilized as a novel electrode. By extending the

recent theory of cyclic voltammetry at porous electrodes to account for interfacial double-layer capacities, nonlinear effects of ohmic resistances, and parasitic reactions, we could quantitatively investigate non-faradaic as well as desired and undesired faradaic current contributions. Combination of experimental and theoretical studies allowed a unique quantitative assessment of the intrinsic catalytic activity of selected electrode materials concerning the $\text{VO}_2^+/\text{VO}^{2+}$ redox reaction.

1. Introduction

Among the available energy storage systems, redox flow batteries (RFB) are promising candidates since the energy and power can be adjusted independently.^[1] In particular, the vanadium redox flow battery (VRFB), which adopts the same element in both positive and negative electrolytes, has been used in large-scale energy storage systems thanks to its unique advantages including long cycle life, high stability, fast response, and no cross contamination of the active species.^[2]

The electrode is an essential element of VRFB as it provides the active sites for the redox reactions and simultaneously facilitates the transport of chemical reactants from the electrolyte.^[3] Carbon felt, graphite felt and carbon paper are the most commonly utilized electrode materials in VRFBs owing to their comparable high chemical durability, electrical conductivity, mechanical stability and their low cost.^[4] However, their poor electrochemical activity and low surface area usually result in high charge/discharge polarization losses during battery

operation. Therefore, further optimization in electrode design by controlling the microstructure and surface chemistry are required in order to develop a VRFB that is capable of achieving a technical and commercial breakthrough.^{[5][5b]} In particular, the modification of carbon-based materials by graphene coating,^[6] metal oxides decoration (e.g. CeO_2 ,^[7] Nd_2O_3 ,^[8] NiO ,^[9] Mn_3O_4 ^[10] and SnO_2 ^[11]) and heteroatoms doping (e.g. oxygen,^[12] chlorine^[13] and nitrogen^[14]) are used.

As a novel concept for alternative electrode materials, electrospun carbon-based fibrous mats are recently explored since their fiber diameter, architecture, and surface area can be readily adjusted.^[15] Electrospinning is an effective approach that provides lightweight nanofibrous electrodes with large surface areas and high porosity that show improved electrochemical activity in VRFB.^[8,15b,16]


In this context, one strategy is to electrospin polyacrylonitrile (PAN) fibers, followed by a carbonization step at high temperature in order to obtain conductive and electrochemically active carbon nanofibrous electrodes. Unfortunately, the performance of these electrospun nanofibers is still unsatisfying and further developments are required to significantly improve their application as electrode in VRFB. For this purpose, an incorporation of carbon nanoparticles into electrospun nanofibers is considered as a reasonable approach to improve their electrochemical behavior. This enhancement effect is assumed to be based on an optimized electrical conductivity as well as an improved intrinsic catalytic activity.^[17] In our previous work, we demonstrated that utilization of carbon black (CB) loaded nanofibrous electrodes could improve the electrochemical performance of these electrospun electrode materials compared to the commercial carbon felt and carbon black-free fibers.^[18] In this manner, polyacrylic acid (PAA) was added as a binder to the electrospinning solution for higher CB loading.^[16b,18] Apart from adding CB, another strategy to possibly increase the electrode performance may be the addition of conductive polymers to the composite. It is already evidenced that they perform well as active electrode materials

[a] Dr. M. Maleki, Dr. T. Tichter, Dr. G. A. El-Nagar, Prof. C. Roth
Institute for Chemistry and Biochemistry
Freie Universität Berlin
14195 Berlin, Germany
E-mail: maleki.m83@gmail.com

[b] Dr. G. A. El-Nagar
Chemistry Department, Faculty of Science
Cairo University
12613 Cairo, Egypt

[c] Dr. G. A. El-Nagar, Dr. I. Lauermaann
Helmholtz-Zentrum Berlin für Materialien und Energie
14109 Berlin, Germany

[d] Prof. C. Roth
Electrochemical Process Engineering, Faculty of Engineering
University of Bayreuth
95447 Bayreuth, Germany

 © 2020 The Authors. ChemElectroChem published by Wiley-VCH GmbH. This is an open access article under the terms of the Creative Commons Attribution Non-Commercial NoDerivs License, which permits use and distribution in any medium, provided the original work is properly cited, the use is non-commercial and no modifications or adaptations are made.

in supercapacitors, fuel cells and as superior binder materials in high-energy lithium-ion batteries.^[19] Conductive polymers combine the attractive properties of the conventional polymers (e.g. good processability and suitable mechanical/thermal/chemical properties) and the unique electronic properties of metals and semiconductors.^[20] This class of materials possesses intrinsic conducting frameworks that promote the transport of charges. They can provide large interfaces between the electronic transporting phase (electrode) and the ionic-transporting phase (electrolyte) facilitating high rate capability. Among them, polyaniline (PANI) is one of the most widely used conductive polymers and known for its excellent thermal stability, high electrical conductivity, and corrosion resistance. Thermal treatment (carbonization) transforms PANi into stable units with modified chemical structure and high electrical conductivity.^[21] Moreover, PANi can be employed as a carbon precursor to fabricate metal free electrodes with high content of nitrogen, which can play an important role in enhancing electrochemical performance.^[22] Nitrogen-doped carbon materials are beneficial as they exhibit more surface active species and defects that facilitate the heterogeneous charge transfer.^[23] These features render PANi as an interesting candidate for electrode materials in various rechargeable electrical energy storage devices alone or when combined with other materials such as Zn,^[24] Nafion,^[25] carbon nanotubes,^[26] graphite,^[27] Ag^[28] and sulfonated poly (ether ether ketone).^[29] On the other hand, incorporating fillers like carbon black as secondary phase is proven to further enhance the physical and (electro)chemical properties of PANi in a wide range of electrical, electrochemical and electronics applications.^[30] However, it has to be underlined that most of the published studies suggest an enhanced electrocatalytic activity utilize cyclic voltammetry (CV) for a qualitative electrochemical characterization of the electrode kinetics only. This experimentally oriented approach is based on comparing peak-to-peak separations, peak height and/or integrated current. Unfortunately, it does not guarantee a proper interpretation of the experimental data due to the inherent ambiguity of CV in porous electrode structures. Nevertheless, since other studies involving non-porous electrodes also highlight the catalytic activity of carbon black (CB), the incorporation of carbon nanoparticles may still be a promising way to increase the electrode performance. Therefore, we adopt this approach for the electrode of vanadium redox-flow system in this study.

Herein, we introduce a simultaneous procedure to fabricate a conductive electrospun composite electrode by introducing a fibrous nanostructure made of polymers (PAN, PAA), conductive linker (PANI) and carbon black (CB). To the best of our knowledge, there is no other report on electrospun nanofibrous composite electrodes, containing PANi and CB in a PAN-based matrix investigated for possible application in VRFB. Fabricated electrodes are characterized by means of scanning electron microscopy (SEM), thermogravimetric analysis (TGA), Raman spectroscopy, X-ray photoelectron spectroscopy (XPS) and cyclic voltammetry (CV). Since cyclic voltammetry of porous electrodes offers significant pitfalls in data interpretation, a sophisticated theoretical model which allows for an in depth electro-

chemical characterization of the 3D nanofibrous conductive mats is created. This particular model represents the further development of the theory presented in our previous publications with emphasis on the vanadium redox flow system.^[31] In this manner, a simultaneous quantitative characterization of capacitive as well as desired and/or undesired Faradaic currents is provided. Based on these findings, we suggest that the electrospun structures proposed in this work can be a suitable electrode material for VRFB related applications with respect to intrinsic catalytic activity as well as electronic conductivity.

2. Results and Discussion

The first task was to optimize the different parameters of the electrospinning process including blending ratio of PAN, PAA, PANi and CB. The total weight concentration of the electrospinning solution was fixed at 10 w/v% to ensure steady electrospinning conditions. A mixture of PAN and PAA was used as polymeric template for CB loading. Two groups of fibers were produced as described in Table 1: I) polymeric nanofibrous mats loaded with 15 wt% CB (without PANi assigned as PAN/PAA/CB) and II) polymeric nanofibrous mats loaded with 15 wt% CB and 15 wt% PANi (referred as PAN/PAA/PANI/CB). These optimized weight ratios resulted in a viscous solution that was suitable for electrospinning. It is worth to mention that solutions containing higher levels of CB and CB/PANI were difficult to spin because of their high viscosity and discontinuity of the flow.

Figure 1 shows selected optical and SEM images of the obtained as-spun PAN/PAA/CB (group I) and PAN/PAA/PANI/CB (group II) fibers. Both groups formed flexible 3D randomly oriented nanofibrous constructs (Figure 1a1).

The estimated mean diameter of the obtained fibers of both groups were 610 ± 165 nm (group I) and 618 ± 275 nm (group II). Despite the mean fiber diameter of both groups that was not significantly different, the fibers decorated with CB/PANI showed a rougher surface compared to the obtained fibers without PANi (Figure 1a3 vs. Figure 1a2).

A more revealing feature of the porous structure can be seen from the STEM image in Figure 2. As shown in Figure 2a2, the as-prepared CB/PANI fibers showed solid fibers with a highly porous surface morphology. Therefore, this CB/PANI loaded fiber might have higher active surface achieved by its nanofibrous morphology and porous structure. Similar behavior was reported by He et al.^[32] for aqueous lithium ion batteries.

The effect of CB and PANi on the thermal stability of the obtained composite nanofibrous materials was investigated by TGA. The changes in the weights of various fibrous mats (i.e. group I and group II) as a function of temperature are plotted

Table 1. Weight ratio of the polymeric/CB matrix to fabricate electrospun nanofibrous composite electrodes.

Sample	PAN	PAA	PANI	CB
PAN/PAA/CB	75 %	10 %	–	15 %
PAN/PAA/PANI/CB	60 %	10 %	15 %	15 %

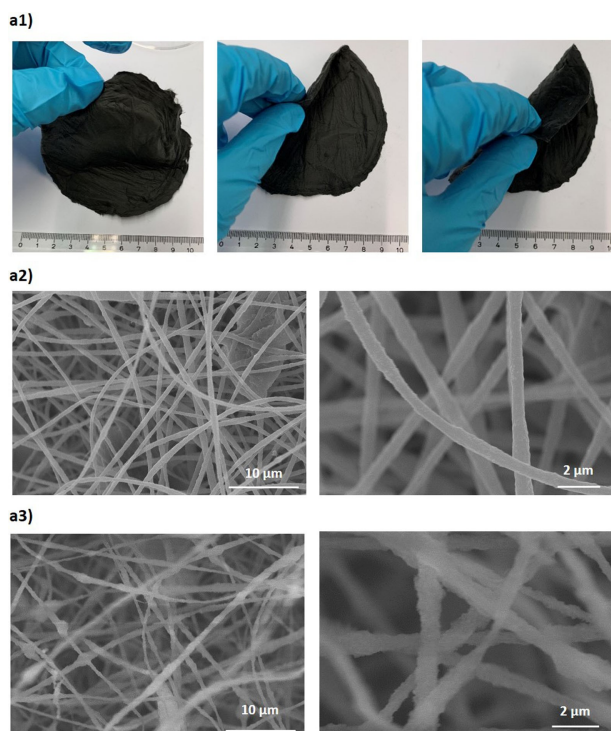


Figure 1. a) Optical image of self-standing as-spun fibrous composite electrode showing its mechanical flexibility; SEM images of as-spun nanofibrous electrodes made of a2) group I (PAN/PAA/CB) and a3) group II (PAN/PAA/PANI/CB).

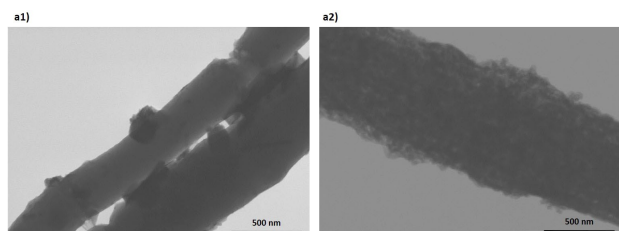


Figure 2. STEM images of as-spun nanofibrous electrodes made of a1) group I (PAN/PAA/CB) and a2) group II (PAN/PAA/PANI/CB).

in Figure 3. A close examination of the TGA data showed an improved thermal stability of the composite fibrous web when

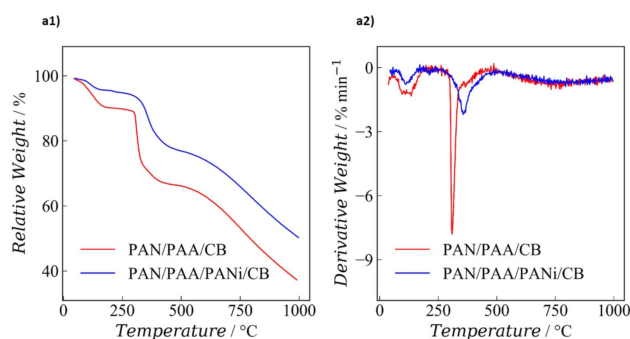


Figure 3. a1) TGA and a2) derivative TGA thermograms of as-spun nanofibrous electrodes for PAN/PAA/CB and PAN/PAA/PANI/CB fibers.

PANi was loaded. In both groups of fibers, a wide endothermic peak was seen with a maximum at around 117 °C, associated with the removal of weakly bound water. The initial decomposition temperature was noted at around 357 °C with nominal weight ratio of 15% for samples loaded with PANi versus 311 °C for the fibrous composite without PANi.

Moreover, the loaded fibrous mat with PANi exhibited an overall weight loss of approximately 50% at around 1000 °C, where the fibers without PANi, lost this value at 790 °C. This effect could be attributed to inhibiting free radical formation in the cyclization pathway due to the presence of PANi in the polymeric matrix which was in agreement with other findings.^[33] Therefore, electrospun fibers loaded with CB/PANi (group II) showed better thermal stability with slower weight loss compared to the fibers loaded with CB only (group I). Our results were in agreement with other findings when PAN/PANi fibrous composite exhibited higher thermal properties as compared to PAN fibers.^[34] The promising thermal properties of the CB/PANi fibrous composite suggested that this material could be a favorable electrode due to its strong interaction between the polymer chains and the CB.

The structure and the density of defects of the as-prepared fiber materials were further examined using Raman spectroscopy. The obtained results are displayed in Figure 4. As clearly seen in this figure, two bands centered at 1330 cm⁻¹ and 1603 cm⁻¹, corresponding to the D-band (disordered portion) and the G-band (ordered graphitic structure) of the carbon-based nanomaterials, were observed for the fibers of both groups (I & II), respectively.

The presence of the strong D band suggested that the carbon component in these as-spun nanofibrous composite had low crystallinity and graphitization which is typical of disordered graphitic material with two Raman bands and was observed by other researchers, too.^[35] To obtain accurate spectroscopic parameters, a curve-fitting procedure with mixed Gaussian/Lorentzian peaks was conducted for the shown Raman spectra of both groups of fibers (Figure 4). The spectroscopic parameters obtained by curve-fitting the peaks are presented in Table 2. The lower I_D/(I_D+I_G) ratio was commonly associated with an ordering and the decrease in the concentration of defects.^[36]

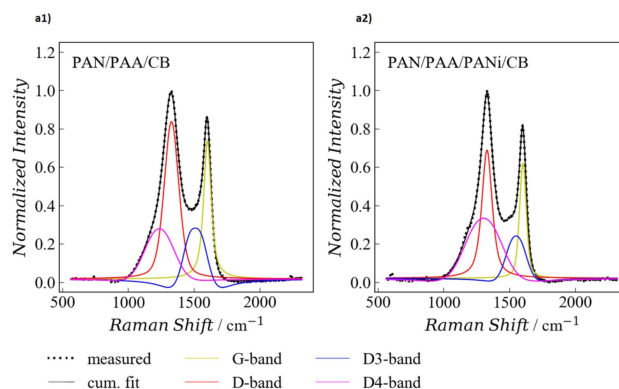


Figure 4. The Raman spectra of the electrospun nanofibrous composite: a1) group I (PAN/PAA/CB) and a2) group II (PAN/PAA/PANI/CB).

Sample	Band	[cm ⁻¹]	I _D /(I _D + I _G)	I _{D3} /(I _{D3} + I _G)	I _{D4} /(I _{D4} + I _G)
PAN/PAA/CB	D	1330	0.65	0.18	0.45
	D3	1510			
	D4	1237			
	G	1603			
PAN/PAA/PANi/CB	D	1329	0.65	0.36	0.63
	D3	1551			
	D4	1304			
	G	1603			

As shown in Figure 4 and Table 2, the electrospun nanofibrous electrodes with and without PANi presented almost the same ratios of the integrated intensity of the D- and G-bands (i.e. ~0.65).

This indicated that there was no significant change in ordering of the carbon black structures in the fibers of the abovementioned groups and both webs were essentially disordered materials in their as-spun form without carbonization.

In general, both samples were lower in intensity of the D3 and D4 bands indicating considerable amounts of amorphous carbon^[37] in their fibrous electrodes. However, significant differences in D3 and D4 band positions were observed between these two groups of samples (PAN/PAA/CB vs. PAN/PAA/PANi/CB). The relative intensity of the D3 band ($I_{D3}/I_G + I_{D3}$), was proposed as a sensitive and reliable indicator to characterize the amount of amorphous carbon.^[38] The D3 band was higher in intensity in the electrospun fibers with CB/PANi (sample PAN/PAA/PANi/CB), indicating considerable amounts of amorphous carbon in this as-spun fibrous composite.

XPS was further used for examining the surface functionalities of the synthesized free-standing carbon nanofibers together with investigating the interaction between the utilized polymers, conductive linker, and carbon black. Figure 5 displays the high resolution spectra of C1s and O1s of the as-spun and carbonized fibers of both groups (PAN/PAA/CB vs. PAN/PAA/PANi/CB).

An attempt was made to fit the C1s and O1s spectra of both groups of electrospun fibrous electrodes as shown in Figure 5 and to assign the main spectral components to species present on the samples. However, it should be emphasized that due to the wide range of binding energies published for identical organic functional groups, this assignment would always be preliminary as long as there is no additional spectroscopic evidence. Furthermore, charging effects on the insufficiently conductive electrospun fibers could lead to a shift to higher B.E. which might explain some of the differences in spectra between as-spun and carbonized samples. As shown in Figure 5, the C1s spectrum of PAN/PAA/CB fibers was deconvoluted into five different peaks assigned to the different carbon species. The peak at 284.9 eV were assigned to the main PAN polymer chain (C–C and C–H) and the other four peaks at 285.9, 287.6, 289.6 and 292.4 eV, were ascribed to C–O, C≡N, C=O and π - π^* , respectively.^[39] Furthermore, the C1s spectrum of PAN/PAA/PANi/CB fibers was also fitted with five different peaks

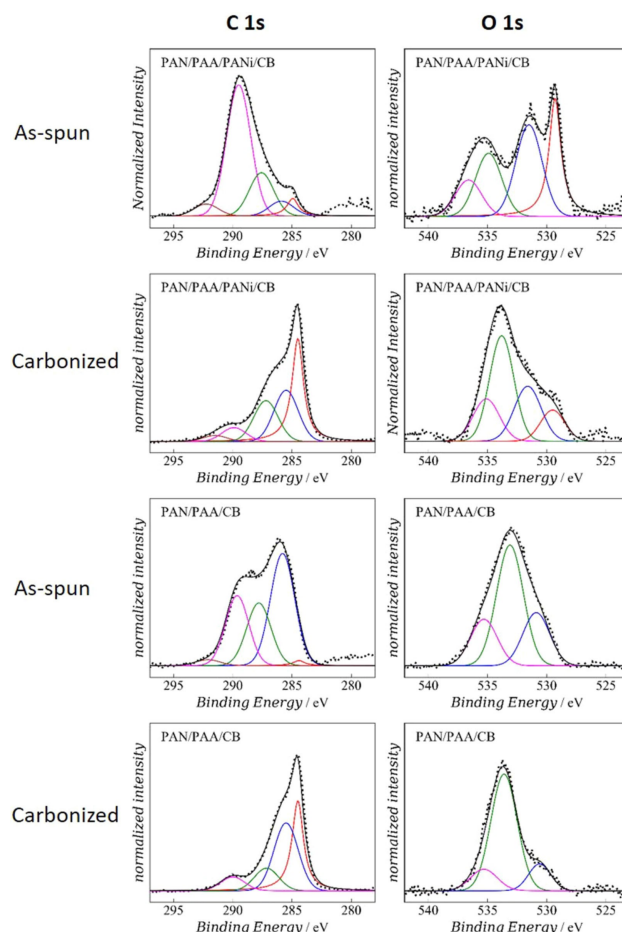


Figure 5. High-resolution C1s and O1s X-ray photoelectron spectra of as-spun and carbonized electrospun fibers made of PAN/PAA/CB and PAN/PAA/PANi/CB.

attributed to C–C and C–H (284.6 eV), C–N or CN (285.9 eV), C–O and C–N⁺ or C=N⁺ (287.6 eV), C–O=C and C=O (289.6 eV) and π - π^* (292.4 eV).^[40] Moreover, an increase of the C–O component in PAN/PAA/CB fibers as a separate peak could be detected which might be associated with better incorporation of CB into the fibers when PANi was not loaded into the polymeric matrix.^[41] Upon carbonization, PAN/PAA/CB and PAN/PAA/PANi/CB fibers showed almost the same fitted peaks. However, the intensity of the C–C/C–H peaks in PAN/PAA/PANi/CB increased after carbonization, suggesting an increase in the fraction of sp²-bonded carbon in the near fiber surface (Figure 5).

Deconvolution of the XPS O1s spectra for as-spun PAN/PAA/CB fibers displayed three main components with binding energies at around 530 (e.g. C=O), 533.2 (e.g. C–OH/C–O–C) and 535.5 eV (e.g. COOH). However, the PAN/PAA/PANi/CB fibers had an extra peak at 536.7 eV that might be due to chemisorbed water.^[42] The O1s XPS spectra of both groups of fibrous composites had a peak at around 530 eV that was caused by C=O groups mainly existing on the surface of fibers. For PAN/PAA/PANi/CB, it became stronger, indicating the content of C=O was increased in these fibers due to good

compatibility between PAN, PAA, PANi and CB. In PAN/PAA/CB fibrous composite, the peak at 533.2 eV became stronger, which might have been caused by the increase of C–O–C and C–O–H groups. As shown in Figure 5, carbonization did not drastically change the peak positions for sample PAN/PAA/CB. However, when PANi was loaded within the fibrous structure, there was a change in fiber surface chemistry of carbonized fibers.

Both groups showed that carbon and oxygen were the most abundant elements at the fibers' surface. However, there were slight changes in binding energies compared to the literature. This could be due to different chemical interactions when CB was present in the fiber structure^[41] and also to charging effects on the insufficiently conductive electrospun fibers as charging could cause shifts to higher B.E. as well as broadening of features.

Apart from the morphological and spectroscopic characterizations, a thorough investigation of the electrochemical performance of these novel electrospun electrode materials was performed by means of diffusional cyclic voltammetry. Since a classical analysis of experimental CV data might provide significant chances of misinterpretation when porous electrode structures are involved, a sophisticated model for data analysis was developed. For this purpose, our previously presented theory of cyclic voltammetry at macroporous electrodes^[31,43] was extended for the VRFBs related parasitic currents (i.e. carbon corrosion, oxygen evolution) as well as the particularly high surface area catalysts related to this work. The effects of capacitive currents and the non-linear contributions of coupled Ohmic resistances were included by following the approach introduced by Montella^[44] which was adopted for porous electrodes in our recent publication.^[45]

2.1. Theory and Derivation

The general assumption of our model was the parallel connection of a capacitance (either ideal or non-ideal, e.g. a constant phase element), a desired Faradaic reaction at any degree of electrochemical reversibility and an electrochemically irreversible parasitic reaction. This equivalent circuit is depicted in Figure 6.

The parasitic reaction (e.g. oxygen evolution or carbon corrosion in positive VRFB reaction) was treated as a diffusion independent quantity. Consequently, a constant surface con-

centration of the depolarizer was assumed. This was considered as a fair assumption, since water was present in huge excess, when compared to the vanadium species in the electrolyte. Therefore, one might directly start with the Laplace transformed version of the current in a potential sweep experiment as proposed by Montella^[44] and indicated in Equation 1.

$$\bar{I}(s) = \frac{\nu C_{CPE}}{s^2(s^{-\gamma} + \tau_{CPE})} + \frac{1}{1 + s^\gamma \tau_{CPE}} \cdot \bar{I}_{far}(s) \quad (1)$$

In Equation 1, ν represents the potential sweep rate, C_{CPE} the ideal or non ideal double layer capacity with the unit of $F \times s^{\gamma-1}$, τ_{CPE} the pseudo time constant of the connection of the solution resistance with the CPE according to

$\tau_{CPE} = R_{sol} \cdot C_{CPE}$, and γ represented the CPE-parameter for the optional deviation from ideal capacitive behaviour ($0 < \gamma \leq 1$). The faradaic current was assumed to be the sum of the desired and the parasitic current. In analogy, this would also hold for the Laplace transformed faradaic current in Equation 1. Consequently, one could write Equation 2:

$$\bar{I}(s) = \frac{\nu C_{CPE}}{s^2(s^{-\gamma} + \tau_{CPE})} + \frac{1}{1 + s^\gamma \tau_{CPE}} \cdot (\bar{I}_{far, des}(s) + \bar{I}_{far, par}(s)) \quad (2)$$

Performing the inverse Laplace transform, we obtained the time dependent current after some rearrangements as indicated in Equation 3:

$$I(t) = I_{CPE}^*(t) + \int_{I_{far, des}(0)}^{I_{far, des}(t)} W(t - \tau) dI_{far, des} + \int_{I_{far, par}(0)}^{I_{far, par}(t)} W(t - \tau) dI_{far, par} \quad (3)$$

In Equation 3, the quantity $I_{CPE}^*(t)$ represents the capacitive current that flows in absence of any faradaic reaction. This current was given by the inverse Laplace transform of the first term in Equations 1 and 2. It can be obtained by means of numerical inverse Laplace transform (e.g. using Talbot's method^[45–46]) or as a generalized Mittag-Leffler function.^[44] The function W in Equation 3 represents the antiderivative of the inverse Laplace transform of the $\frac{1}{1+s^\gamma \tau_{CPE}}$ term in Equation 3 (this quantity is readily accessible as $\mathcal{L}^{-1}\left(\frac{1}{s(1+s^\gamma \tau_{CPE})}\right)(t)$, since division by s in the Laplace domain represents an integration in the time domain). This function can also be evaluated by means of numerical inverse Laplace transformation. For this purpose, we utilized the modified Talbot contour proposed by Dingfelder and Weideman.^[46b] The purely faradaic current of the desired reaction in the porous network was obtained by exploiting the model described in our previous publications,^[31,43] corrected by the solution resistance. The parasitic current (also corrected by the solution resistance) is assumed to follow the relation shown in Equation 4:

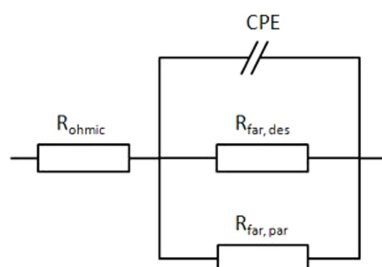


Figure 6. Modified Randles circuit accounting for an additional parasitic reaction.

$$I_{far,par}(t) = nFAk^0 c_{H_2O} \exp\left(\frac{\alpha_{par} nF(E(t) - E_{par}^0 - R_{ohm} \cdot I(t))}{RT}\right) \quad (4)$$

With this knowledge, solving the integral Equation 3 was the most crucial step at this stage. It could be performed numerically by approximating the integrals as Riemann-Stieltjes integrals. Therefore, one might discretize the time variables in increments of δ , so that $t = i\delta$ and $\tau = j\delta$. In this manner, we could finally obtain Equation 5:

$$0 = -I(t) + I_{CPE}^*(t) + \sum_{j=0}^{i-2} W((i-j)\delta) [I_{far,des}((j+1)\delta) - I_{far,des}(j\delta)] + W(\delta) [I_{far,des}(i\delta) - I_{far,des}((i-1)\delta)] + \sum_{j=0}^{i-2} W((i-j)\delta) [I_{far,par}((j+1)\delta) - I_{far,par}(j\delta)] + W(\delta) [I_{far,par}(i\delta) - I_{far,par}((i-1)\delta)] \quad (5)$$

Equation 5 represents a recurrence relation along which the values of $I(t)$ can be obtained successively. However, since $I_{far,des}$ as well as $I_{far,par}$ both require some knowledge on the total current in order to account for an ohmic drop, equation 5 cannot be solved directly in terms of $I(t)$. Consequently, numerical root-finding was utilized to obtain the total current in this case. For this purpose, we utilized the f -solve function of the python module (scipy.optimize). Following this routine, the values of $I_{far,des}$ and $I_{far,par}$ were obtained subsequently to $I(t)$. The remaining capacitive current was then calculated via $I_{CPE}(t) = I(t) - I_{far,des} - I_{far,par}$. Before starting another iteration, all these three current values were stored in the computer memory, since they were mandatory for solving the recurrence sums in equation 5. By following this procedure, it was readily seen that one could unravel the capacitive, the desired and the parasitic current contributions of an electroanalytical experiment. Such a knowledge is exceptionally valuable for analyzing experimental CV curves like the one that we obtained for the electrospun nanofibrous electrodes in this paper. In order to evaluate experimental results, we restricted ourselves to the manual CV fitting routine outlined in our previous work.^[31]

Following the mentioned strategy, Figure 7 depicts the experimental and simulated CV curves of the electrospun nanofibers of both groups utilized as electrode at the scan rate of 2 mVs^{-1} . From Figure 7 the significant correlation between faradaic and capacitive currents could be observed.

This behavior could be interpreted as follows: At the foot of the CV wave, the entire current was approximately capacitive since all faradaic reactions contributed a comparably high charge transfer resistance. However, as soon as the potential increased, the rate of the electron transfer also increased. Consequently, the electric current was more likely to pass through the faradaic pathway. Therefore, the capacitive current decreased around the CV peak. Finally, once the parasitic

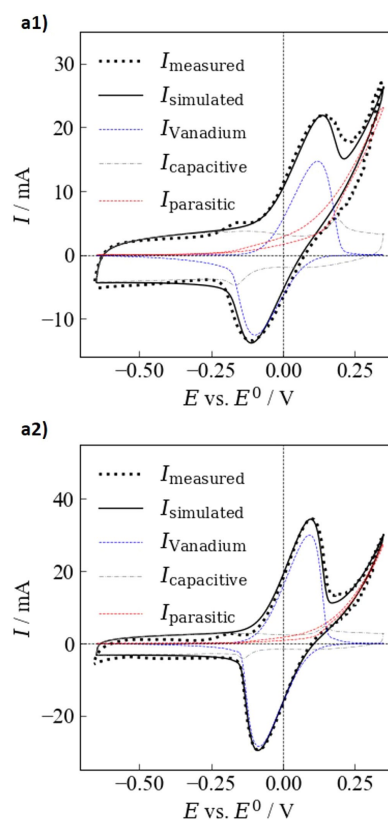


Figure 7. Experimentally acquired (dots) and simulated (solid curve) cyclic voltammograms of electrospun fibrous electrode for a1) group I (PAN/PAA/CB) and a2) group II (PAN/PAA/PANI/CB) utilized as catalyst for the electrochemical $\text{VO}_2^+/\text{VO}^{2+}$ redox reaction CV curves were sampled at a potential sweep rate of 2 mVs^{-1} .

current rose, the capacitive current as well as the desired Faradaic current was being depleted since the current was more likely to flow through the undesired pathway owing to the least charge transfer resistance at larger overpotentials. In other words, the pure presence of a parasitic reaction could suppress the desired Faradaic reaction even without changing the actual electrode kinetics.

Bearing this complex interplay of individual current contributions in mind, and taking into account that in case of a porous electrode the random-network diffusion also significantly influences the CV response, it could be concluded that comparing peak positions and height would certainly lead to entirely ambiguous results. In contrast, by fitting the respective CV curves according to our model, we could provide valuable insights into the reaction kinetics of desired and parasitic reactions as well as parasitic current contributions simultaneously. Following the outlined idea in this work, the fitting results reported in Table 3 are obtained.

The obtained results demonstrated that the electrospun-based electrodes with incorporated PANi exhibit a noticeable improvement in the electrochemical activity towards the $\text{VO}_2^+/\text{VO}^{2+}$ reactions with clear distinguished redox peaks.

From the fitting results given in Table 3, it can be seen, that the PAN/PAA/PANI/CB fibers show a significantly enhanced

Table 3. Parameters used for fitting the CV curves depicted in Figure 7.

Sample	k_{des}^0 cm^{-1}	α_{des}	k_{par}^0 cm^{-1}	α_{par}	A cm^2	R_{ohm} Ω	$\frac{C_{CPE}}{F \times s^{-1}}$
PAN/PAA/CB	5.5×10^{-5}	0.5	5.8×10^{-8}	0.23	35	3.7	0.77
PAN/PAA/PANI/CB	1.5×10^{-3}	0.55	2.1×10^{-8}	0.27	65	1.9	0.57

electron transfer kinetics when compared to the PAN/PAA/CB sample, since the standard rate constant for the desired vanadium redox-reactions was increased by two orders of magnitude. This inherent increase in the catalytic activity might be correlated with the presence of different surface functional groups (as suggested by XPS results, see Figure 5) that could act as catalytically active sites. Moreover, this could reduce charge transfer resistance and improve electrical conductivity. This phenomenon is in good agreement with reports by other researchers, too.^[23,32]

Taking a look at the capacitive part of the CV, it could be seen that no significant changes were present between the PAN/PAA/CB and the PAN/PAA/PANI/CB samples. Such a behavior appears to be reasonable, as the electrode area exposed to the electrolyte might not change substantially. However, at this stage it is worth to note that the active electrode area is not necessarily equal to the exposed electrode area (the boundary of electrode/electrolyte) but to the number of catalytically active sites available for an electrochemical reaction.

Therefore, it could be shown that the PAN/PAA/PANI/CB fibrous electrode provided about twice the electrochemically active area. This could be associated with the enhanced electrical conductivity introduced by the PANi which allows to connect the active sites in the electrode surface more efficiently. In addition, the combined contributions from both PANi and CB structures and their internal interactions should be taken into account. This is in agreement with Bavio et al^[47] who reported that introducing CB particles in the PANi nanostructure remarkably improved their electrochemical behavior.

In this context, it was also not surprising that the ohmic resistance was lowered by a factor of two approximately. In this way, the PANi/CB network led to an easier charge transfer at the fibrous electrode/electrolyte interface as well as a higher conductivity of the obtained fibers which had a positive effect on the electrochemical properties. A similar finding was reported by Wu et al^[40a] for PANi/CB films.

These findings underline the exceptional importance of the electrode conductivity and furthermore demonstrate that the electrode area is not necessarily correlated with the electrochemically active electrode area. Regarding the rate constants of the parasitic reactions, it could be seen that the PAN/PAA/PANI fibrous composite had a lower tendency for the side reactions. However, in this context it could not be clarified whether the parasitic reaction corresponded to the oxygen evolution or to the carbon corrosion. However, if it corresponds to carbon corrosion, the lowered parasitic current could be explained by an enhanced stability of the electrode material. Regarding the results obtained from the TGA analysis (see

Figure 3), this scenario appears reasonable as PAN/PAA/PANI/CB had better stability. However, the lowered parasitic current could also be attributed to suppressed oxygen evolution kinetics. Nevertheless, attributing the changed electrokinetic activity for parasitic currents would be entirely speculative at this stage. To conclude, our results indicate that PANi can act as a linker to connect the loaded CB particles and to facilitate the electron transfer.

3. Conclusions

We established that the electrospun composites, based on polyaniline (PANi) and carbon black (CB), displayed consistent and promising electrochemical properties. The PANi/CB was intended to ensure that the interior of the utilized polymers and CB particles was electronically addressable, and to provide alternative reaction sites for the redox reaction at the surface of the fibers. Moreover, PANi can act as a carbon source to link the loaded CB particles within nanofibers and make them available for an increased $\text{VO}_2^+/\text{VO}^{2+}$ redox reaction. Studying the surface morphology of the resulting electrospun fibers by SEM and STEM showed that the fibers were uniform with nanoscale diameters. The overall thermal stability of the composite electrode was enhanced, when PANi/CB was implemented in the structure of our fibrous composite. We demonstrated that the PANi/CB loaded electrospun composite electrode improved the electrochemical performance of the PAN-based nanofibers compared to the CB loaded fibers. Our XPS findings indicated that carbon and oxygen elements were bonded differently when PANi/CB was loaded into the electrospun fibers compared to the CB-loaded fibers. We also presented a refined theoretical model for an in depth electrochemical characterization of these 3D nanofibrous conductive composites with emphasis on the vanadium redox flow system. In this manner, we could unravel the capacitive, the desired and the parasitic current contributions of an electroanalytical experiment. This knowledge is extraordinary valuable for analyzing experimental CV curves like the ones we obtained for the electrospun nanofibrous electrodes, since the kinetics of all individual current contributions can be quantified simultaneously. Furthermore, our results highlight the exceptional importance of the electrospun electrode conductivity on the electrochemical performance. Since our strategy captures a plethora of electrochemical circumstances, the present findings can mark a new route to improve the performance of conductive electrospun-based composite electrodes for VRFBs.

Experimental Section

Materials

Polyacrylonitrile (PAN; Mw 150,000), polyacrylic acid (PAA; Mw 450,000) and polyaniline-carbon black composite (PANi-CB; 20 wt% polyaniline on carbon black) were purchased from Sigma-Aldrich, Germany. Carbon Black (CB-XCmax;) was received from Cabot. N, N-dimethyl formamide (DMF; $\geq 99.5\%$, C₃H₇NO) and N-Methyl-2-pyrrolidone (NMP; $\geq 99.8\%$, C₅H₉NO) were purchased from Carl Roth, Germany.

Fabrication of Nanofibrous Electrode by Electrospinning

The spinning solvent was a mixture of N, N-dimethyl formamide (DMF) and N-Methyl-2-pyrrolidone (NMP) with ratio of 80: 20 (v:v) and solutions were prepared by overnight stirring of polymer and solvent. The dispersion of carbon black (CB) and the dissolution of the PAN-PAA-PANi composite system for electrospinning were performed in DMF: NMP at room temperature. All sample preparations were carried out under ambient conditions. Electrospinning was done utilizing a commercial unit (IME Technology, EC-DIG).

The electrospinning solution was placed in a 2 mL luer lock syringe (B-Braun, Germany) equipped with a blunt 21-gauge needle mounted on a syringe pump. The syringe pump was used to provide a constant stream of solution at the tip of the needle. The electrical potentials of +15 kV and -2 kV were applied to the needle and collector by a positive and a negative power supply, respectively. Fibers were collected at a distance of 14 cm from the needle on a 40 mm-diameter grounded copper disk. Spinning was done under ambient conditions: subsequently, fibrous mats were vacuum dried for a day. The collected electrospun fibers were stabilized by heating them to 280 °C with a heating ramp of 1 °Cmin⁻¹. The temperature was held for 1 h in an open tube in a conventional furnace (split tube furnace EST 12/300, Carbolite Ltd). The stabilized fibers were then carbonized under a nitrogen flow by heating them to 1000 °C at a rate of 5 °Cmin⁻¹ and the temperature was held for 1 h.

Characterization of Electrospun Nanofibrous Composite Electrode

Fiber and mat morphologies were analyzed via scanning electron microscopy (SEM; Hitachi UHR FE-SEM SU8030) after gold sputter coating (Safematic CCU-010 HV) of the samples for 30 s (~5 nm). The average and standard deviation of the fiber diameters were measured by choosing 100 fibers and analyzing them using IMAGEJ software (v.1.52a, National Institute of Health, USA). Scanning transmission electron microscopy (STEM-in-SEM) was conducted at an operating acceleration voltage of 30 kV. STEM samples were prepared by directly depositing the as-spun fibers on a carbon-coated copper grid.

Electrochemical characterization by means of cyclic voltammetry (CV) was performed in a three-electrode compartment utilizing a Galvanostat/Potentiostat Reference 600 (Gamry Instruments). The working electrode consisted of a 8 mg of the electrospun sample sandwiched between two glassy carbon plates (Sigradur, HTW). A commercial carbon felt (SGL GFA 6 EA) was used as a counter electrode and a saturated calomel electrode (SCE) served as reference electrode. The cell was equipped with 0.2 molL⁻¹ vanadium (51% V³⁺ and 49% V⁴⁺) in 2 molL⁻¹ H₂SO₄ supporting electrolyte. CV measurements were performed over a potential range from 0.2 to 1.2 V at a scan rate of 2 mVs⁻¹.

Raman spectroscopy was performed with a REN-ISAW via Raman spectrometer with a Leica microscope using 633 nm laser as an excitation source, 60× optical lens and streamline mode to gain more detailed information about the surface defects of the as-prepared electrospun nanofibers. Deconvolution of the spectra was performed by mixed Gaussian/Lorentzian peaks to describe both the main D- and G-bands and the two minor ones D3 and D4 using Origin Pro 2017.

The thermal stability of the fabricated mats was investigated with thermogravimetric analysis (TGA; Netzsch STA 449F5). The runs were performed in the presence of argon, at a heating rate of 10 °C/min, and at temperatures ranging from room temperature to 1000 °C.

X-ray photoelectron spectroscopy (XPS, CLAM4 electron analyzer from Thermo VG scientific), using non-monochromatic Mg K α X-ray source (1253.6 eV) was used to determine the surface composition and chemistry. The X-ray power of 150 W (10 kV, 15 mA) was used for all analyses. The measurements were performed in vacuum < 10⁻⁹ Pa. Elemental high resolution scans were collected with a 20 eV pass energy for the C1s and O1s core levels. For evaluation, a S-shaped background was subtracted, and peaks were fitted using a combination of Gaussian and Lorentzian lines with variable proportions for each component of the same element. The gold 4f_{7/2} peak set to a binding energy of 84 eV was used for energy calibration.

Acknowledgements

This work was funded by the German Federal Ministry for Economic Affairs and Energy (Bundesministerium für Wirtschaft und Energie (BMWi) under grant 03ET6130B (HiCo-BiPEC). Open access funding enabled and organized by Projekt DEAL.

Conflict of Interest

The authors declare no conflict of interest.

Keywords: electrospinning · nanofibrous electrodes · carbon black · polyaniline · VO₂⁺/VO₂²⁺ redox reactions

- [1] a) R. A. Potash, J. R. McKone, S. Conte, H. D. Abruña, *J. Electrochem. Soc.* **2016**, *163*, A338-A344; b) A. Z. Weber, M. M. Mench, J. P. Meyers, P. N. Ross, J. T. Gostick, Q. Liu, *J. Appl. Electrochem.* **2011**, *41*, 1137.
- [2] a) M. Rychcik, M. Skyllas-Kazacos, *J. Power Sources* **1988**, *22*, 59–67; b) G. Kear, A. A. Shah, F. C. Walsh, *Int. J. Energy Res.* **2012**, *36*, 1105–1120.
- [3] a) L. Hua, C. Shou wen, Y. Chuan wei, *Electrochemistry* **2002**, *8*, 258–259; b) Á. Cunha, J. Martins, N. Rodrigues, F. Brito, *Int. J. Energy Res.* **2015**, *39*, 889–918.
- [4] a) H. Kaneko, K. Nozaki, Y. Wada, T. Aoki, A. Negishi, M. Kamimoto, *Electrochim. Acta* **1991**, *36*, 1191–1196; b) K. J. Kim, M.-S. Park, Y.-J. Kim, J. H. Kim, S. X. Dou, M. Skyllas-Kazacos, *J. Mater. Chem. A* **2015**, *3*, 16913–16933.
- [5] a) A. Forner-Cuenca, F. R. Brushett, *Curr. Opin. Electrochem.* **2019**, *18*, 113–122; b) M. Gencten, Y. Sahin, *Int. J. Energy Res.* **2020**.
- [6] a) L. Xia, Q. Zhang, C. Wu, Y. Liu, M. Ding, J. Ye, Y. Cheng, C. Jia, *Surf. Coat. Technol.* **2019**, *358*, 153–158; b) D. O. Opar, R. Nankya, J. Lee, H. Jung, *Electrochim. Acta* **2020**, *330*, 135276.
- [7] M. Jing, X. Zhang, X. Fan, L. Zhao, J. Liu, C. Yan, *Electrochim. Acta* **2016**, *215*, 57–65.

- [8] A. Fetyan, G. A. El-Nagar, I. Derr, P. Kubella, H. Dau, C. Roth, *Electrochim. Acta* **2018**, *268*, 59–65.
- [9] N. Yun, J. J. Park, O. O. Park, K. B. Lee, J. H. Yang, *Electrochim. Acta* **2018**, *278*, 226–235.
- [10] A. Di Blasi, C. Busacca, O. Di Blasia, N. Briguglia, G. Squadrito, V. Antonucci, *Appl. Energy* **2017**, *190*, 165–171.
- [11] S. Mehboob, G. Ali, H.-J. Shin, J. Hwang, S. Abbas, K. Y. Chung, H. Y. Ha, *Appl. Energy* **2018**, *229*, 910–921.
- [12] Z. Jiang, V. Alexandrov, *ACS Appl. Mater. Interfaces* **2020**, *3*, 7543–7549.
- [13] H. Gursu, M. Gençten, Y. Şahin, *Int. J. Energy Res.* **2018**, *42*, 3303–3314.
- [14] H. Gursu, M. Gençten, Y. Şahin, *Int. J. Energy Res.* **2018**, *42*, 3851–3860.
- [15] a) G. Wei, J. Liu, H. Zhao, C. Yan, *J. Power Sources* **2013**, *241*, 709–717; b) A. Fetyan, I. Derr, M. K. Kayarkatte, J. Langner, D. Bernsmeier, R. Kraehnert, C. Roth, *ChemElectroChem* **2015**, *2*, 2055–2060; c) Y. Yang, F. Simeon, T. A. Hatton, G. C. Rutledge, *J. Appl. Polym. Sci.* **2012**, *124*, 3861–3870.
- [16] a) Z. He, M. Li, Y. Li, J. Zhu, Y. Jiang, W. Meng, H. Zhou, L. Wang, L. Dai, *Electrochim. Acta* **2018**, *281*, 601–610; b) A. Fetyan, J. Schneider, M. Schnucklake, G. A. El-Nagar, R. Banerjee, N. Bevilacqua, R. Zeis, C. Roth, *ChemElectroChem* **2019**, *6*, 130–135; c) Z. Zhang, B. Bai, L. Zeng, L. Wei, T. Zhao, *Energy Technol.* **2019**, *7*, 1900488.
- [17] a) M. N. Hyder, R. Kaviani, Z. Sultana, K. Saetia, P.-Y. Chen, S. W. Lee, Y. Shao-Horn, P. T. Hammond, *Chem. Mater.* **2014**, *26*, 5310–5318; b) A. V. Murugan, T. Muraliganih, A. Manthiram, *Chem. Mater.* **2009**, *21*, 5004–5006.
- [18] G. A. E.-N. Mahboubbeh Maleki, Denis Bernsmeier, Jonathan Schneider, Christina Roth, *Sci. Rep.* **2020**, *10*, 1–14.
- [19] a) J. Huang, K. Wang, Z. Wei, *J. Mater. Chem.* **2010**, *20*, 1117–1121; b) Y. Hou, Y. Cheng, T. Hobson, J. Liu, *Nano Lett.* **2010**, *10*, 2727–2733; c) F. Meng, Y. Ding, *Adv. Mater.* **2011**, *23*, 4098–4102; d) F. Cheng, W. Tang, C. Li, J. Chen, H. Liu, P. Shen, S. Dou, *Chem. Eur. J.* **2006**, *12*, 3082–3088; e) K. S. Park, S. B. Schougaard, J. B. Goodenough, *Adv. Mater.* **2007**, *19*, 848–851.
- [20] Y. Shi, L. Peng, Y. Ding, Y. Zhao, G. Yu, *Chem. Soc. Rev.* **2015**, *44*, 6684–6696.
- [21] J. J. Langer, S. Golczak, *Polym. Degrad. Stab.* **2007**, *92*, 330–334.
- [22] H. Wang, J. Lin, Z. X. Shen, *J. Sci. Adv. Mater. Dev.* **2016**, *1*, 225–255.
- [23] Z. He, Y. Jiang, J. Zhu, H. Wang, Y. Li, H. Zhou, W. Meng, L. Dai, L. Wang, *Electrochim. Acta* **2018**, *279*, 279–288.
- [24] Y. Zhao, S. Si, C. Liao, *J. Power Sources* **2013**, *241*, 449–453.
- [25] S. Tan, D. Belanger, *J. Phys. Chem. B* **2005**, *109*, 23480–23490.
- [26] D. Zhang, Y. Yin, C. Liu, S. Fan, *Chem. Commun.* **2015**, *51*, 322–325.
- [27] K. Ghanbari, M. F. Mousavi, M. Shamsipur, H. Karami, *J. Power Sources* **2007**, *170*, 513–519.
- [28] S. Wu, Y. Zhao, D. Li, Y. Xia, S. Si, *J. Power Sources* **2015**, *275*, 305–311.
- [29] O. David, K. Percin, T. Luo, Y. Gendel, M. Wessling, *J. Energy Storage* **2015**, *1*, 65–71.
- [30] a) K. Wu, T. Ting, G. Wang, W. Ho, C. Shih, *Polym. Degrad. Stab.* **2008**, *93*, 483–488; b) F. G. Souza Jr, L. Sirelli, R. C. Michel, B. G. Soares, M. H. Herbst, *J. Appl. Polym. Sci.* **2006**, *102*, 535–541.
- [31] T. Tichter, J. Schneider, D. Andrae, M. Gebhard, C. Roth, *ChemPhysChem* **2020**, *21*, 428–441.
- [32] Z. He, Y. Jiang, W. Meng, J. Zhu, Y. Liu, L. Dai, L. Wang, *Electrochim. Acta* **2016**, *222*, 1491–1500.
- [33] E. Cam, N. Aladag Tanik, I. Cerkez, E. Demirkan, Y. Aykut, *J. Appl. Polym. Sci.* **2018**, *135*, 45567.
- [34] G. Bayramoğlu, M. Karakışla, B. Altıntaş, A. U. Metin, M. Saçak, M. Y. Arica, *Process Biochem.* **2009**, *44*, 880–885.
- [35] L. Ji, X. Zhang, *Carbon* **2009**, *47*, 3219–3226.
- [36] M. Rose, Y. Korenblit, E. Kockrick, L. Borchardt, M. Oschatz, S. Kaskel, G. Yushin, *Small* **2011**, *7*, 1108–1117.
- [37] C. Sheng, *Fuel* **2007**, *86*, 2316–2324.
- [38] M. Pawlyta, J.-N. Rouzaud, S. Duber, *Carbon* **2015**, *84*, 479–490.
- [39] M. Wu, Q. Wang, K. Li, Y. Wu, H. Liu, *Polym. Degrad. Stab.* **2012**, *97*, 1511–1519.
- [40] a) G. Wu, L. Li, J.-H. Li, B.-Q. Xu, *Carbon* **2005**, *43*, 2579–2587; b) J. Ren, X. Huang, N. Wang, K. Lu, X. Zhang, W. Li, D. Liu, *Synth. Met.* **2016**, *222*, 255–266.
- [41] L. M. da Silva, H. G. Lemos, S. F. Santos, R. A. Antunes, E. C. Venancio, *Mater. Today Commun.* **2018**, *16*, 14–21.
- [42] a) B. Strzemiescka, A. Voelkel, J. Donate-Robles, J. M. Martín-Martínez, *Appl. Surf. Sci.* **2014**, *316*, 315–323; b) P. Singh, K. Pal, *Electrochim. Acta* **2020**, 136719.
- [43] T. Tichter, D. Andrae, J. Mayer, J. Schneider, M. Gebhard, C. Roth, *Phys. Chem. Chem. Phys.* **2019**, *21*, 9061–9068.
- [44] C. Montella, *J. Electroanal. Chem.* **2012**, *667*, 38–47.
- [45] T. Tichter, D. Andrae, J. Schneider, M. Gebhard, A. Hilger, I. Manke, C. Roth, *Electrochim. Acta* **2020**, 136487.
- [46] a) A. Talbot, *J. Inst. Math. Its Appl.* **1979**, *23*, 97–120; b) B. Dingfelder, J. Weideman, *Numer. Algorithms* **2015**, *68*, 167–183.
- [47] M. A. Bavio, G. G. Acosta, T. Kessler, *Int. J. Hydrogen Energy* **2014**, *39*, 8582–8589.

Manuscript received: November 6, 2020

Accepted manuscript online: December 14, 2020